AIAA JOURNAL
Vol. 44, No. 5, May 2006

New Scheme for the Computation of Compressible Flows

Adnan Qamar,* Nadeem Hasan,* and Sanjeev Sanghi†
Indian Institute of Technology, Delhi, New Delhi 110 016, India

A new approach for the computation of unsteady compressible flows has been developed. The new scheme employs upwinding of the convective flux based on particle velocity and has been termed the particle velocity upwinding (PVU) scheme. The PVU scheme is an explicit two-step predictor–corrector scheme, in which the convective fluxes are evaluated on cell faces using a first-order upwinding method. The scheme is accurate and stable, giving solutions free from oscillations near the discontinuities without any explicit addition of artificial viscosity. The PVU scheme has an edge over state-of-the-art high-resolution schemes in terms of simplicity of implementation in multidimensional flows and problems involving complex domains. The numerical scheme is validated for both Euler and Navier–Stokes equations. Furthermore, the PVU scheme is used to investigate laminar supersonic viscous flow over a forward-facing step. The results are obtained for $M_\infty = 1.5$–3.5 in steps of 0.5 and for $Re_\infty = 10^4$. Step heights H_s of 10 and 20% of the characteristic length of the problem are considered. The effect of step height and the incoming freestream Mach number on the spatial flow structure and on the important design parameters such as wall pressure, skin friction, heat transfer, and length of separated region are investigated.

Nomenclature

C_f	=	skin-friction coefficient
C_H	=	Stanton number
C_v	=	specific heat at constant volume
E	=	nondimensional total energy
e	=	nondimensional specific internal energy
H	=	nondimensional step height
H_s	=	dimensional step height
K_∞	=	freestream thermal conductivity
k	=	nondimensional thermal conductivity
L	=	characteristic length
M_∞	=	freestream Mach number
P_W	=	nondimensional wall pressure
p	=	nondimensional pressure
p_∞	=	freestream pressure
Re_∞	=	freestream Reynolds number
T	=	nondimensional temperature
T_∞	=	freestream temperature
U_∞	=	freestream velocity
u, v	=	nondimensional velocity components in x and y direction, respectively
x, y	=	Cartesian coordinates
γ	=	specific heat ratio
Δt	=	time increment
μ	=	nondimensional viscosity
ρ	=	nondimensional density
ρ_∞	=	freestream density

I. Introduction

An important aspect of the design of supersonic aircraft is the minimization of aerodynamic and thermal loads onto the vehicle's surface. Unfortunately local contour discontinuities are generally unavoidable in the design, although a smooth aerodynamic shape of the surface is attempted. Examples of such discontinuities occur at positions where control devices and the intake of the propulsion system are integrated.

Generic geometries of these contour discontinuities are, for example, kinks, fins, windshield, door edges, compression or expansion corners, and forward- or backward-facing steps. These geometries will induce shock wave/boundary-layer interactions and the flow separation from the surface, resulting in an increase of pressure and heat flux level in the vicinity of the obstacle at supersonic speeds. Local pressure fluctuations around such obstacles generate noise, with audio-frequency intensity more than 100 times greater than those due to boundary-layer turbulence over a smooth surface. The occurrence of such interaction over the surface may deteriorate the aerodynamic efficiency, making the control of the vehicle critical. A common geometry that often occurs on the vehicle surface is the forward-facing step. The flow characteristic around forward-facing step is an important part of the vehicle design. Thus, in the present work, a numerical investigation is carried out to determined the flow characteristic around a forward-facing step.

In the past, many researchers have carried out theoretical experimental and numerical studies concerning the effect of such geometries. Previous theoretical treatment of the shock/boundary-layer interaction problem consists in solving a boundary-layer equation together with a coupling equation relating the development of the inner viscous flow to the outer flow. The governing partial differential equations can be solved by finite difference techniques[1] or can be expressed as integral relations[2] and solved as ordinary differential equations. This treatment, in general, involves the question of uniqueness because a certain portion of the flowfield contains a substantial upstream influence and the initial and downstream boundary conditions cannot be completely specified. In some integral methods techniques, there is also a question of the so-called jump conditions from supercritical to subcritical types of boundary layers.

Solution of the full Navier–Stokes equations across the complete flow domain avoids these issues and removes some restrictive assumptions such as the static pressure being constant across the boundary layer and the interaction of viscous and inviscid flows only along a line at or near the edge of boundary layer, which is difficult to define in a supersonic flow.

Chapman et al.[3] carried out an extensive experimental investigation of supersonic flow past a forward-facing step. The main aim of the investigation was to study the phenomena of the flow separation and transition. The scope of measurement encompassed Mach numbers between 0.4 and 3.6 and Reynolds numbers, based on length in front of the step, between 4×10^3 and 5×10^6. The principal variable controlling the pressure distribution in separated flows was found to be the location of transition relative to the reattachment and separation positions. Classification was made of each separated flow into three regimes: pure laminar, transitional, and turbulent. The general result regarding the steadiness of flow and the influence of

Received 6 December 2004; revision received 16 October 2005; accepted for publication 17 October 2005.

*Research Scholar, Department of Applied Mechanics. Student Member AIAA.
†Associate Professor, Department of Applied Mechanics.

Reynolds number within each regime was also investigated. The work of Chapman et al. involved the exploration with step heights that are small. The ratio of step height to length in front of the step varied from 0.01 to 0.1.

Li et al.[4] performed an experimental investigation of hypersonic flow over a set of rectangular cylinders mounted over a flat surface. All of the tests were carried out at Mach 5 under turbulent conditions. The results indicate that the aspect ratio (H/W) is an important parameter for the classification of the flowfield. Efimtsov et al.[5] carried out a series of experimental investigations on the TU-144LL Flying Laboratory and obtained flight-test data of the pressure fluctuation field in front of a forward-facing step and behind a backward-facing step. The flight test covered a Mach number range of 0.57–1.97.

Carter[6] obtained a numerical solution of the Navier–Stokes equations for laminar supersonic flow past a 10-deg compression corner at Mach 3.0 using an adiabatic thermal condition at the solid wall. Hung and MacCormack[7] developed an efficient time-splitting, second-order accurate, numerical scheme that was used to solve the complete Navier–Stokes equation for supersonic and hypersonic laminar flow over a two-dimensional compression corner. Favorable comparisons with previous calculations and with experimental results were made. Their results indicate that the pressure profile is neither constant across the boundary layer nor constant along simple straight characteristic lines, as had been assumed in some previous analyses.

Grotowsky and Ballmann[8] performed a numerical investigation of hypersonic step flow. A multiblock finite volume method was used to discretize all spatial derivatives appearing in the balance equations. A second-order Godunov-type method was utilized for the nondiffusive part of the governing equations, whereas central differences were used for the diffusive part. Time integration was performed via a second-order implicit scheme. Results were obtained for Mach 7.94 and were compared with experimental results.

From the present literature review, note that the detailed numerical study of the forward-facing step in supersonic ranges has not been carried out. The effect of step height greater than 10% of the characteristic length has not been reported in the literature. Also for the lower step height, important design parameters such as heat transfer coefficient and skin-friction coefficient have not been reported. Thus, the primary effort of this work is to carry out detailed studies of the forward-facing step to determine the important design parameters for Mach number ranging from 1.5 to 3.5 and the two step heights equal to 10 and 20% of the characteristic length of the problem.

Another important contribution of this paper is the development of a two-step predictor-corrector, particle velocity upwinding (PVU) scheme, with first-order upwinding applied to calculate the convective flux, yielding a stable and accurate scheme. The primary motivation for the development of a simple, stable, and accurate scheme for multidimensional compressible flows governed by the Navier–Stokes equations is that most of the higher-order flux-based schemes utilize some sort of switches called flux limiters in region of the steep gradient to reduce the order of the schemes and to stabilize the solution. The detection of the region of steep gradient and the subsequent design of switches is a complex issue for multidimensional flows. Wave-based schemes, which are generally superior to the flux-based schemes for the Euler equation, are also not very suitable for computing multidimensional flows governed by Navier–Stokes equations. This is because of two reasons. First, the Navier–Stokes equations, being hyperbolic–elliptic in character, do not have a complete wave description. Second, the inviscid part of the Navier–Stokes equations does not posses a unique characteristic or wave representation, as suggested by Laney.[9] A state-of-the-art method, such as the reconstruction–evolution method, uses a piecewise polynomial to approximate the solution over the flow domain. The construction of a piecewise polynomial is a computationally expensive task, especially in multidimensional flows. Furthermore, these schemes require special treatment near the boundary points. Thus, the PVU scheme is a step toward devising a stable and accurate scheme that is simple from the implementation point of view, especially for flows involving multiple space dimensions.

The scheme is validated for various test cases: 1) two one-dimensional shock tube problems (Sod's problem) governed by a one-dimensional unsteady Euler equation and 2) supersonic flow past a 10-deg compression corner governed by the full Navier–Stokes equations. As indicated by validation studies of the one-dimensional shock tube problem and the compression corner problem, the PVU scheme captures shocks faithfully without the addition of any artificial viscosity. The boundary treatment of the PVU scheme is also very simple in comparison to wave-based schemes.

The paper is organized as follows. In Sec. II, the physical model and its mathematical representation is described. Subsequently, in Sec. III, the numerical method employed for the simulation is described. In Sec. IV, the stability of the scheme is demonstrated. Section V contains the validation studies. The results and discussion of the forward-facing step problem are in Sec. VI Finally conclusions drawn from the study are presented in Sec. VII.

II. Governing Equations

The conservation laws[10] are formulated in a two-dimensional space with Cartesian coordinates. The nondimensional forms of the governing equations expressed in strong conservation vector notation are as follows:

$$\frac{\partial \boldsymbol{U}}{\partial t} + \frac{\partial \boldsymbol{F}}{\partial x} + \frac{\partial \boldsymbol{G}}{\partial y} = \boldsymbol{J} \tag{1}$$

where $\boldsymbol{U}$, $\boldsymbol{F}$, $\boldsymbol{G}$, and $\boldsymbol{J}$ are column vectors given by

$$\boldsymbol{U} = \begin{Bmatrix} \rho \\ \rho u \\ \rho v \\ \rho E \end{Bmatrix} \tag{2}$$

$$\boldsymbol{F} = \begin{Bmatrix} \rho u \\ \rho u^2 + \dfrac{p}{\gamma M_\infty^2} - \dfrac{\mu}{Re_\infty}\left(\dfrac{4}{3}\dfrac{\partial u}{\partial x} - \dfrac{2}{3}\dfrac{\partial v}{\partial y}\right) \\ \rho uv - \dfrac{\mu}{Re_\infty}\left(\dfrac{\partial v}{\partial x} + \dfrac{\partial u}{\partial y}\right) \\ \rho uE - \left(\dfrac{\gamma}{Pr_\infty Re_\infty}\right)k\dfrac{\partial T}{\partial x} + (\gamma - 1)up + \phi_F \end{Bmatrix} \tag{3}$$

$$\boldsymbol{G} = \begin{Bmatrix} \rho v \\ \rho uv - \dfrac{\mu}{Re_\infty}\left(\dfrac{\partial v}{\partial x} + \dfrac{\partial u}{\partial y}\right) \\ \rho v^2 + \dfrac{p}{\gamma M_\infty^2} - \dfrac{\mu}{Re_\infty}\left(\dfrac{4}{3}\dfrac{\partial v}{\partial y} - \dfrac{2}{3}\dfrac{\partial u}{\partial x}\right) \\ \rho vE - \left(\dfrac{\gamma}{Pr_\infty Re_\infty}\right)k\dfrac{\partial T}{\partial y} + (\gamma - 1)vp + \phi_G \end{Bmatrix} \tag{4}$$

$$\boldsymbol{J} = \begin{Bmatrix} 0 \\ 0 \\ \dfrac{-\rho g L}{U_\infty^2} \\ \dfrac{-\gamma(\gamma - 1)M_\infty^2}{U_\infty^2}\rho v L g \end{Bmatrix} \tag{5}$$

In Eqs. (2–5),

$$\phi_F = \frac{\gamma(\gamma - 1)M_\infty^2}{Re_\infty}\left[\frac{2}{3}\mu u\left(\frac{\partial v}{\partial y} - \frac{2\partial u}{\partial x}\right) - \mu v\left(\frac{\partial v}{\partial x} - \frac{\partial u}{\partial y}\right)\right] \tag{6}$$

$$\phi_G = \frac{\gamma(\gamma - 1)M_\infty^2}{Re_\infty}\left[\frac{2}{3}\mu v\left(\frac{\partial u}{\partial x} - \frac{2\partial v}{\partial y}\right) - \mu u\left(\frac{\partial v}{\partial x} - \frac{\partial u}{\partial y}\right)\right] \tag{7}$$

and E is nondimensional total energy defined as

$$E = e + \gamma(\gamma - 1)M_\infty^2(\boldsymbol{V}^2/2) \tag{8}$$

The various flowfield variables are nondimensionalized as follows:

$$u = \bar{u}/\boldsymbol{U}_\infty, \qquad v = \bar{v}/\boldsymbol{U}_\infty, \qquad p = \bar{p}/P_\infty, \quad T = \bar{T}/T_\infty$$
$$\rho = \bar{\rho}/\rho_\infty, \qquad \mu = \bar{\mu}/\mu_\infty, \qquad k = \bar{k}/K_\infty, \qquad E = \bar{E}/C_V T_\infty$$
$$e = \bar{e}/C_V T_\infty, \qquad t = \bar{t}\boldsymbol{U}_\infty/L, \qquad x = \bar{x}/L, \qquad y = \bar{y}/L$$

The subscript ∞ represents the incoming freestream conditions, the overbar, values represent the corresponding dimensional values, and L is some appropriate reference length, which for the case of the forward-facing step is the entire length of the computational domain. The preceding system comprises four equations, namely, the continuity, x-momentum, y-momentum, and energy equations. The other complimentary state equations, in their nondimensional form, are as follows.

Equation of state:

$$p = \rho T \tag{9}$$

Sutherland's law of viscosity:

$$\mu(T) = T^{\frac{3}{2}}\left[\left(T_\infty + S^*\right)\Big/\left(TT_\infty + S^*\right)\right] \tag{10}$$

with $S^* = 123.6$ K.

The calorically perfect gas assumption leads to

$$e = T \tag{11}$$

The thermal conductivity is computed by assuming a constant Prandtl number, which for air is $Pr_\infty = 0.716$.

III. Numerical Procedure

The Navier–Stokes equations in their strong conservative form are discretized using a finite difference methodology on a structured grid in a Cartesian coordinate system. The nondimensional form of the governing equations expressed in vector notation is written in a slightly different form as

$$\frac{\partial \boldsymbol{U}}{\partial t} + \frac{\partial(\boldsymbol{F}^c + \boldsymbol{F}^d)}{\partial x} + \frac{\partial(\boldsymbol{G}^c + \boldsymbol{G}^d)}{\partial y} = \boldsymbol{J} \tag{12}$$

The flux vectors $\boldsymbol{F}$ and $\boldsymbol{G}$ are split into two parts, the convective part and the diffusive part. The convective part consist of the convective flux in each equation, where as all other parts of $\boldsymbol{F}$ and $\boldsymbol{G}$ vectors (pressure term, viscous terms, and other terms) are included in the diffusive part. Thus, in terms of vector notation,

$$\boldsymbol{F}^c = \begin{Bmatrix} \rho u \\ \rho u^2 \\ \rho uv \\ \rho uE \end{Bmatrix}$$

$$\boldsymbol{F}^d = \begin{Bmatrix} 0 \\ \dfrac{p}{\gamma M_\infty^2} - \dfrac{\mu}{Re_\infty}\left(\dfrac{4}{3}\dfrac{\partial u}{\partial x} - \dfrac{2}{3}\dfrac{\partial v}{\partial y}\right) \\ -\dfrac{\mu}{Re_\infty}\left(\dfrac{\partial v}{\partial x} + \dfrac{\partial u}{\partial y}\right) \\ -\left(\dfrac{\gamma}{Pr_\infty Re_\infty}\right)k\dfrac{\partial T}{\partial x} + (\gamma - 1)up + \phi_F \end{Bmatrix} \tag{13}$$

$$\boldsymbol{G}^c = \begin{Bmatrix} \rho v \\ \rho uv \\ \rho v^2 \\ \rho vE \end{Bmatrix}$$

$$\boldsymbol{G}^d = \begin{Bmatrix} 0 \\ -\dfrac{\mu}{Re_\infty}\left(\dfrac{\partial v}{\partial x} + \dfrac{\partial u}{\partial y}\right) \\ \dfrac{p}{\gamma M_\infty^2} - \dfrac{\mu}{Re_\infty}\left(\dfrac{4}{3}\dfrac{\partial v}{\partial y} - \dfrac{2}{3}\dfrac{\partial u}{\partial x}\right) \\ -\left(\dfrac{\gamma}{Pr_\infty Re_\infty}\right)k\dfrac{\partial T}{\partial y} + (\gamma - 1)vp + \phi_G \end{Bmatrix} \tag{14}$$

Equation (12) is marched in time using a predictor–corrector strategy. The solution vector at any point (i, j) of the Cartesian grid is obtained at the new time level $(n + 1)$ through the following predictor and corrector steps.

Predictor step:

$$\boldsymbol{U}^* = \boldsymbol{U}^n - \Delta t\left\{\left(\delta_x \boldsymbol{F}^c\right)_{i,j}^n + \left(\delta_x^+ \boldsymbol{F}^d\right)_{i,j}^n + \left(\delta_y \boldsymbol{G}^c\right)_{i,j}^n + \left(\delta_y^+ \boldsymbol{G}^d\right)_{i,j}^n - \boldsymbol{J}^n\right\} \tag{15}$$

Corrector step:

$$\boldsymbol{U}^{n+1} = (\boldsymbol{U}^* + \boldsymbol{U}^n)/2 - \tfrac{1}{2}\Delta t\left\{\left(\delta_x \boldsymbol{F}^c\right)_{i,j}^* + \left(\delta_x^- \boldsymbol{F}^d\right)_{i,j}^* + \left(\delta_y \boldsymbol{G}^c\right)_{i,j}^* + \left(\delta_y^- \boldsymbol{G}^d\right)_{i,j}^* - \boldsymbol{J}^*\right\} \tag{16}$$

where $\delta_{()}^+$, $\delta_{()}^-$, and $\delta_{()}$ are the forward, backward, and central differencing operators, respectively, with the central differencing operator calculating the difference between $i + \frac{1}{2}$ and $i - \frac{1}{2}$ values.

The convective flux terms are evaluated on cell faces using a first-order convective upwinding. Because the upwinding of the convective fluxes is based on the particle velocity at the cell face, the scheme has been named the PVU scheme,

$$\boldsymbol{F}_{i-\frac{1}{2},j}^c = \begin{cases} u_{i-\frac{1}{2},j}\phi_{i-1,j}^F, & \text{if} \quad u_{i-\frac{1}{2},j} \geq 0 \\ u_{i-\frac{1}{2},j}\phi_{i,j}^F, & \text{if} \quad u_{i-\frac{1}{2},j} < 0 \end{cases}$$

where

$$\phi^F = \begin{Bmatrix} \rho \\ \rho u \\ \rho v \\ \rho E \end{Bmatrix}$$

The particle velocity at cell face $u_{i-1/2,j}$ is computed via linear interpolation from the adjacent nodes. The pressure and the viscous terms are treated together, which comprises the diffusive part $\boldsymbol{F}^d$. The x derivative terms appearing in $\boldsymbol{F}^d$ are differenced in the direction opposite to that used for $\partial \boldsymbol{F}^d/\partial x$, whereas the y derivative terms are approximated with central differences. Likewise, the y-derivative terms appearing in $\boldsymbol{G}^d$ are differenced in the direction opposite to that used for $\partial \boldsymbol{G}^d/\partial y$, whereas the x-derivative terms are approximated with central differences.

The proposed PVU scheme is a simple and stable scheme for computation of multidimensional flows governed by Euler and Navier–Stokes equations. The present scheme captures the discontinuities quite well, without any explicit addition of artificial viscosity, thus, producing solutions that are free from oscillatory behavior near the discontinuities. The stability of the PVU scheme is further demonstrated in the following section.

IV. Stability

A numerical scheme is said to be stable if it does not allow errors to be amplified without bound as the solution is marched from one time step to another. The errors may grow indefinitely to "blow" out the solution or may show up locally in the formation of oscillations, overshoots, or undershoots. Therefore, a scheme is stable if the error introduced at a given time level is not amplified as the solution is marched forward in time and locally spurious numerical phenomena such as oscillations, overshoots, and undershoots are minimized. There are various techniques for studying the stability of the scheme. However, as pointed out in Ref. 11, even for simple problems and schemes, the algebra involved may be too cumbersome and may not lead to analytic conditions on the parameters of the scheme to ensure stability. For nonlinear problems, there is a severe lack of theoretical ideas, and in actual practice one follows a combination of two different approaches, namely, 1) linear analysis and 2) numerical experimentation.

In the linear analysis approach, a linear equation is used and discretized using the given scheme. Then the stability conditions are derived using appropriate methods such as the Von Neumann method, the energy method, and the matrix method. The stability analysis is followed by the checking of the monotonicity preservation condition of the scheme. The numerical experimentation approach is generally used for nonlinear problems. The numerical solutions are computed on a sequence of meshes of decreasing mesh size. The behavior of the numerical solution is observed as the mesh is refined. The availability of the exact solution can be very useful in assessing the performance of the numerical method.

Because the PVU scheme is developed for the solution of the nonlinear partial differential equation, the stability of scheme is studied in the similar fashion as just discussed. First, a linear analysis is performed in which the stability condition for the linear advection equation is determined, followed by checking of the monotonicity condition. Furthermore, numerical experimentation is carried out for the solution of scalar conservation laws for which the exact solution is known. Important properties such as convergence, total variation diminishing (TVD), monotonocity, and range-diminishing properties are demonstrated through numerical experimentation, which ensures the stability of PVU scheme.

A. Linear Analysis

For the linear analysis of the PVU scheme, the following model scalar advection equation is chosen:

$$\frac{\partial u}{\partial t} + a\frac{\partial u}{\partial x} = 0 \tag{17}$$

where a is a constant and can be negative or positive. Equation (17) is commonly referred to as the linear advection equation. The linear advection governs the evolution of a single right-running ($a > 0$) or left-running wave ($a < 0$). The proposed PVU scheme comprises two steps, namely, the predictor step and the corrector step. Therefore, to do the Von Neumann linear stability analysis (VNS) analysis, one needs to write the scheme in one step for Eq. (17) that can be done with a little algebraic manipulation. With $a > 0$, the predictor step for Eq. (17) at i and $i-1$ nodes can be written as

$$u_i^* = u_i^n - (c/2)\left(u_i^n - u_{i-1}^n\right) \tag{18}$$

$$u_{i-1}^* = u_{i-1}^n - (c/2)\left(u_{i-1}^n - u_{i-2}^n\right) \tag{19}$$

where $c = a\Delta t/\Delta x > 0$.

Now the corrector step can be written as

$$u_i^{n+1} = \left[\left(u_i^* + u_i^n\right)/2\right] - (c/2)\left(u_i^* - u_{i-1}^*\right) \tag{20}$$

When Eqs. (18) and (19) are substituted in Eq. (20), the final corrector step for $a > 0$ becomes

$$u_i^{n+1} = \beta_1 u_i^n + \beta_2 u_{i-1}^n + \beta_3 u_{i-2}^n \tag{21}$$

Similarly, for $a < 0$, the final corrector step can be written as

$$u_i^{n+1} = \beta_4 u_i^n + \beta_5 u_{i+1}^n + \beta_6 u_{i+2}^n \tag{22}$$

where

$$\beta_1 = \tfrac{1}{2}[(1-c)^2 + 1], \qquad \beta_2 = \tfrac{1}{2}[c(1-c)], \qquad \beta_3 = \tfrac{1}{2}c^2 \tag{23}$$

$$\beta_4 = \tfrac{1}{2}[(1+c)^2 + 1], \qquad \beta_5 = -[c(1+c)], \qquad \beta_6 = \tfrac{1}{2}c^2 \tag{24}$$

Now at a given time interval n, the solution at the ith node can be decomposed into discrete Fourier series as

$$u_i^n = \sum_{m=-N/2}^{N/2} C_m^n \exp(2\pi \mathrm{Im} i/N) \tag{25}$$

Let $\phi_m = 2\pi m/N$.

Because each of the Fourier series coefficient changes by exactly the same factor at every time step, Eq. (25) in terms of amplification factor G_m can be written as

$$u_i^n = \sum_{m=-N/2}^{N/2} (G_m)^n \exp(I\phi_m i) \tag{26}$$

Because the problem is linear, the different Fourier modes do not interact and the equation governing the evolution of any particular mode remains the same. Hence, the stability can be studied by considering the equation of a general mode identified by the phase ϕ. Thus, the contribution by Fourier mode identified by its phase ϕ can be expressed as

$$u_i^n = G^n \exp(I\phi i), \qquad -\pi < \phi < \pi \tag{27}$$

When Eq. (27) is substituted in Eqs. (21) and (22), the amplification factor can be expressed for $a > 0$ as

$$G = (\beta_1 + \beta_2 \cos\phi + \beta_3 \cos 2\phi) - I(\beta_2 \sin\phi + \beta_3 \sin 2\phi) \tag{28}$$

and for $a < 0$ as

$$G = (\beta_4 + \beta_5 \cos\phi + \beta_6 \cos 2\phi) + I(\beta_5 \sin\phi + \beta_6 \sin 2\phi) \tag{29}$$

For stability, $|G|^2 \le 1$. The region of stability and instability can be determined graphically by plotting the neutral curve $|G(\phi, c)|^2 = 1$. Figures 1a and 1b show the neutral curve and the region of stability and instability on the $c-\phi$ plane for $a > 0$ and $a < 0$, respectively. For $a > 0$, it is found that the scheme is unconditionally stable for $0 \le c \le 1$, whereas the scheme is conditionally stable for $c > 1$. For $a < 0$, the unconditional stability condition is $-1 \le c \le 0$. Thus, the overall stability condition for the PVU scheme is $|c| \le 1$ for the linear advection equation.

Once the stability condition is determined, we proceed to determine whether or not the scheme is monotone for the linear advection equation. For this purpose, the theorem on the monotonocity of the scheme is employed.[11]

Theorem: A scheme

$$u_i^{n+1} = \sum_{k=-k_L}^{k_R} \beta_k u_{i+k}^n$$

for the linear advection equation is monotone if and only if the coefficients β_k are nonnegative, that is, $\beta_k \ge 0$.

For the linear advection equation, the coefficients β_k for $a > 0$ and $a < 0$ are given in Eqs. (23) and (24). It can be seen that for $a > 0$ the coefficients β_1, β_2, and β_3 are nonnegative within the stable domain $0 \le c \le 1$ for $a > 0$. Similarly, $(\beta_4, \beta_5, \beta_6) > 0$ when $-1 \le c \le 0$ for $a < 0$. Thus, the PVU scheme is monotone for both $a > 0$ and $a < 0$ within the stability regime determined through the VNS analysis.

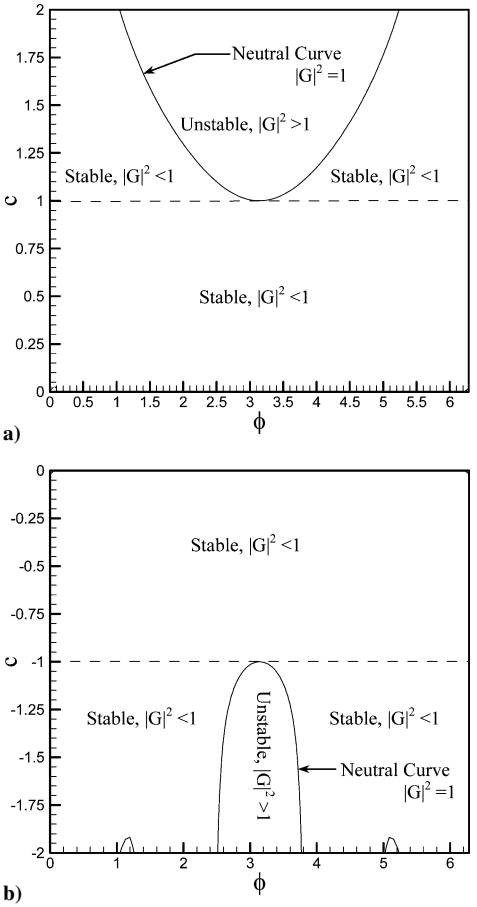

Fig. 1 Neutral curves separating stable and unstable regions of numerical scheme for linear advection equation for a) $a > 0$ and b) $a < 0$.

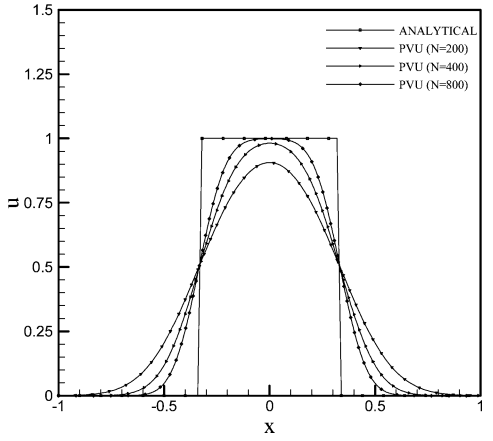

Fig. 2 Numerical and exact solution for linear advection equation at $t = 4$.

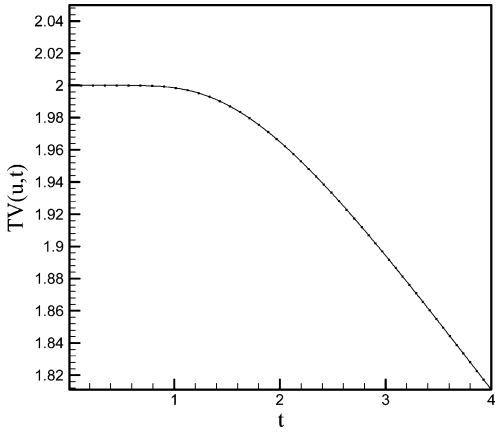

Fig. 3 Decrease of total variation of solution of linear advection equation with respect to time.

B. Numerical Experimentation

The linear stability of the scheme has been investigated by considering the linear advection equation. Because the scheme is intended for nonlinear problems, the issue of nonlinear stability also needs to be addressed. The issue of nonlinear stability is often investigated through numerical test or experiments on nonlinear conservation laws. In this regard, scalar conservation laws are a good choice because they do not exhibit physical instability and, therefore, any observed instability is readily identified as a numerical phenomenon. The two important scalar conservation laws are the linear advection equation, which models simple entropy wave and contacts, and the nonlinear Burgers equation, which models acoustics wave and shocks. The stability and robustness of the scheme have been proved numerically by carrying out the numerical solution of the scalar conservation laws on different grids with decreasing mesh size. The convergence and TVD properties as reported in Ref. 11 are shown.

1. Linear Advection Equation

Consider the following scalar problem governed by the linear advection equation:

$$\frac{\partial u}{\partial t} + \frac{\partial u}{\partial x} = 0, \qquad -1 \le x \le 1 \tag{30}$$

together with the initial condition given as

$$u(x,0) = \begin{cases} 1, & \text{for} \quad |x| < \frac{1}{3} \\ 0, & \text{for} \quad \frac{1}{3} < |x| < 1 \end{cases} \tag{31}$$

The domain $[-1, 1]$ is periodic. This periodic domain is considered to eliminate the effect of boundary conditions. Figure 2 shows the exact and the computed results for Eq. (30) at $t = 4$. The solution is computed using a sequence of progressively finer grids ($N = 200$, 400, and 800) with $c = 0.8$ up to $t = 4$. In the time interval [0, 4], the initial condition travels around the periodic domain $[-1, 1]$ exactly twice so that $u(x, 4) = u(x, 0)$. The two jump discontinuities in the solution correspond to the contact discontinuities. This test case illustrates progressive contact smearing and dispersion. The numerical results show that as the grid size is reduced the solution converges to the exact solution. The results for the same problem for some of the popular schemes may be found in Ref. 9. The results of these schemes also show a similar behavior. The amount of clipping encountered in these schemes is also similar to that of the PVU scheme.

The TVD property of the PVU scheme is studied by plotting the total variation (TV) $\mathrm{TV}(u, t)$ defined as

$$\mathrm{TV}(u^n) = \sum \left| u_{i+1}^n - u_i^n \right| \tag{32}$$

for every time step.

For the scheme to posses the TVD character, it must satisfy the following inequality:

$$\mathrm{TV}(u^{n+1}) \le \mathrm{TV}(u^n), \qquad \forall n \tag{33}$$

Figure 3 shows $\mathrm{TV}(u, t)$ for $N = 200$ with time. It can be seen that with the passage of time the TV decreases in a monotone fashion. Thus, the scheme exhibits TVD character for the linear advection equation. Also the range of diminishing property of the scheme is also satisfied because maxima do not increase, minima do not decrease, and no new extrema are created with time,[9] which is the actual requirement of range diminishing property.

2. Inviscid Burgers Equation

The inviscid Burgers equation is given by

$$\frac{\partial u}{\partial t} + u\frac{\partial u}{\partial x} = 0 \tag{34}$$

or in conservative form

$$\frac{\partial u}{\partial t} + \frac{\partial}{\partial x}\left(\frac{u^2}{2}\right) = 0 \tag{35}$$

The Burgers equation is solved numerically for three different grids ($N = 200$, 400, and 800) with decreasing mesh size for $c = 0.8$ and for the initial condition given in Eq. (31). The jump from 0 to 1 at $x = -\frac{1}{3}$ creates an expansion fan, whereas the jump from 1 to 0 at $x = \frac{1}{3}$ creates a shock. The solution comprises a sonic point. Although the exact solution never crosses the sonic point, a numerical method with spurious overshoots or oscillations may cross the sonic point once or even several times, causing a dramatic error if the numerical method has a sonic point problem. Figure 4 shows a comparison of the solution obtained by the PVU scheme with the analytic solution at $t = 0.6$. The solution obtained does not show any oscillatory behavior. As the grid size is decreased, the solution converges, thus, indicating the convergence of the scheme for the nonlinear case. The TVD and the range-diminishing properties are also very well satisfied for the nonlinear Burgers equation. Figure 5 shows TV(u, t) for $N = 200$ with time. It can be seen that as the time progresses the TV decreases and no new maxima or minimum are formed, thus, indicating that the range-diminishing condition is satisfied.

Thus, it can be inferred that the PVU scheme is stable and monotone for both linear and nonlinear cases. The robustness and the accuracy of the scheme are further demonstrated via the validation of the scheme, through two standard benchmark problems of a shock tube and a compression corner in the next section.

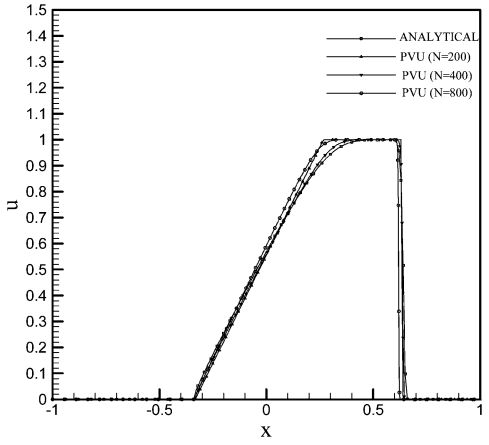

Fig. 4 Numerical and exact solutions for inviscid Burgers equation at $t = 0.6$.

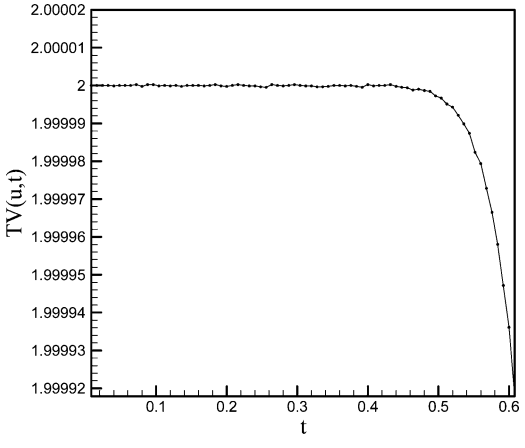

Fig. 5 Decrease of total variation of solution of inviscid Burgers equation with respect to time.

V. Validation Studies

In this section, the validation studies are presented. The scheme has been tested on two benchmark test cases. The first problem comprises two test cases for a one-dimensional shock tube problem (Sod's problems) governed by one-dimensional unsteady Euler equations. The second problem considered is that of supersonic flow past a 10-deg compression corner governed by the full Navier–Stokes equations. For all of the cases, the ratio of specific heats γ is 1.4 and the gas constant $R = 287$ J/(kg · K). All of the results are for laminar flow, and no turbulence model has been used.

A. One-Dimensional Shock Tube Problems (Sod's Problems)

The one-dimensional shock tube problems, suggested by Sod,[12] often appear in modern research papers for validation purpose. The problems are governed by the one-dimensional, unsteady Euler equations given as

$$\frac{\partial \boldsymbol{U}}{\partial t} + \frac{\partial \boldsymbol{F}^c}{\partial x} + \frac{\partial \boldsymbol{F}^d}{\partial x} = 0 \tag{36}$$

where

$$\boldsymbol{U} = \begin{Bmatrix} \rho \\ \rho u \\ \rho E \end{Bmatrix}, \qquad \boldsymbol{F}^c = \begin{Bmatrix} \rho u \\ \rho u^2 \\ \rho u E \end{Bmatrix}, \qquad \boldsymbol{F}^d = \begin{Bmatrix} 0 \\ p \\ up \end{Bmatrix} \tag{37}$$

The spatial domain of the problem is taken to be the interval $[-10, 10]$. Each half of the solution domain contains a fluid initially at rest. However, the pressure and density are different on either side of $x = 0$. The flow is then allowed to evolve in time, leading to the formation of shock, expansion, and contact discontinuities in the solution domain. The initial values of the variables on the left and right of $x = 0$ for the two test cases are given as follows.

Case 1:

$$\rho_L = 1\,\text{kg/m}^3, \qquad u_L = 0\,\text{m/s}, \qquad P_L = 100{,}000\,\text{N/m}^2$$

$$\rho_R = 0.125\,\text{kg/m}^3, \qquad u_R = 0\,\text{m/s}, \qquad P_R = 10{,}000\,\text{N/m}^2$$

Case 2:

$$\rho_L = 1\,\text{kg/m}^3, \qquad u_L = 0\,\text{m/s}, \qquad P_L = 100{,}000\,\text{N/m}^2$$

$$\rho_R = 0.01\,\text{kg/m}^3, \qquad u_R = 0\,\text{m/s}, \qquad P_R = 1000\,\text{N/m}^2$$

For computation, uniform grids of 100, 200, 400, and 800 points with time step of $\Delta t = 1 \times 10^{-5}$ s are employed. Figures 6 and 7 show a comparison of the pressure, velocity, density, entropy, speed of sound, and Mach number profiles with the analytical results for two Sod's problems at time $t = 0.01$ s. As discussed in Ref. 9, test case 1 does not contain a strong shock, contact or expansion, and it does not have sonic point. The only thing that makes the test case 1 challenging is that the shock and the contact discontinuity are close together (Fig. 6c). Even at the final time $t = 0.01$, when their separation is greatest, the shock and contact are separated by only 2.5 m. Test case 2 is much more challenging than test case 1. First, the shock and contact are still separated by a small distance. Second, the expansion fan contains an expansive sonic point $u - a = 0$ at $x = 0$ as seen in Figs. 7b and 7f. Third, the shock contains a compressive sonic point $u + a = 0$, and finally, the initial condition involves a large pressure ratio of 100.

The results obtained from the PVU scheme are in good agreement with analytical results. The scheme captures the shock and expansion reasonably accurately. Also, the PVU scheme captures the sonic points perfectly without any special treatment in the scheme, which is often done in wave-based schemes.[13,14] These test problems prove the ability of the present PVU scheme to capture the discontinuities without any oscillatory behavior or severe overshoots and

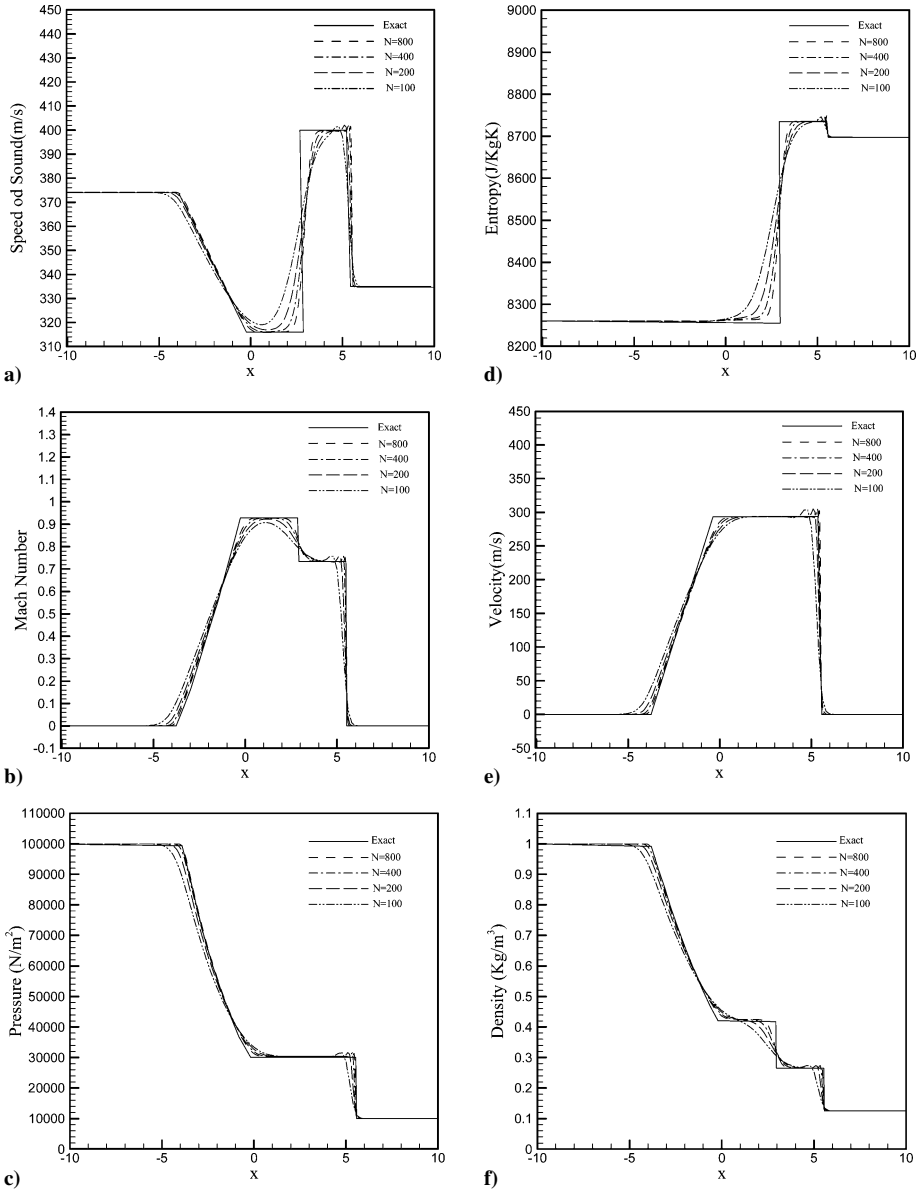

Fig. 6 Structure of flowfield at $t = 0.01$ for test case 1.

undershoots without any addition of explicit artificial viscosity. The scheme also captures the extremum values quite well, except for test case 2 in the Mach number profile (Fig. 7f), where there is a clipping of about 5% from the actual peak value. The contact discontinuity is significantly smeared over several grid points, which is clear in the density plot (Fig. 7f). It can be seen that as the grid size is decreased the numerical solution converges toward the exact solution in both the cases. The smearing in the contact discontinuity is also reduced as the grid size is reduced. The smearing of contact discontinuity for the two test cases is a challenging problem as also observed for some of the popular first-order schemes such as Van Leer's flux vector splitting,[15] Roe's first-order upwinding,[16] Gudunov's first-order upwinding,[17] and Harten's first-order upwinding[13] schemes.

B. Supersonic Flow past the 10-Degree Compression Corner

As a second test case, a supersonic two-dimensional viscous flow past the 10-deg compression corner has been studied. This problem has been studied by several researchers.[7,18,19] In the present work, the results have been compared with the numerical study by Hung and MacCormack.[7] The comparison is made for $Re_\infty = 1.68 \times 10^4$ and $M_\infty = 3.0$. The computational domain spans the x direction from $x = -0.2$ to $x = 1.8$ and the y direction from $y = 0$ to $y = 0.575$. The leading edge of the flat plate is placed at $x = 0$ and the 10-deg corner at $x = 1.0$. At the inflow, all of the flowfield variables are specified. On the solid surface (plate and compression ramp), the no-slip condition is specified on the velocity and the wall temperature is taken to be equal to the freestream stagnation temperature. Symmetry conditions are specified on the line of symmetry at $y = 0$ for $x < 0$. At the outflow boundary, the second derivative of pressure, and the first derivatives of velocity and temperature have been set equal to zero in a direction parallel to the ramp. At the top exit boundary, the first derivative of all of the flowfield variables in the y direction are assumed to be zero. The freestream Reynolds number Re_∞ is based on the distance between the leading edge of the plate and the compression corner. The dependence of the viscosity on the temperature is modeled via Sutherland's law of viscosity. Fine nonuniform mesh spacing of $\Delta y = 8 \times 10^{-4}$ is used in the region near the wall for resolving the viscous layer and is gradually expanded to a coarse equally spaced mesh $\Delta y = 1 \times 10^{-2}$ in the outer region, where viscous effects are negligible. A mesh of 330×205 is utilized to compute the solution. Figures 8a–8d show the contours of steady-state pressure, temperature, Mach number, and streamtrace patterns, respectively. The leading-edge shock due to the development of boundary layer on the flat plate has been captured quite well. The separation of the flow ahead of the corner and its subsequent reattachment downstream of the corner results in a small region of recirculation that can be observed in the solution, as

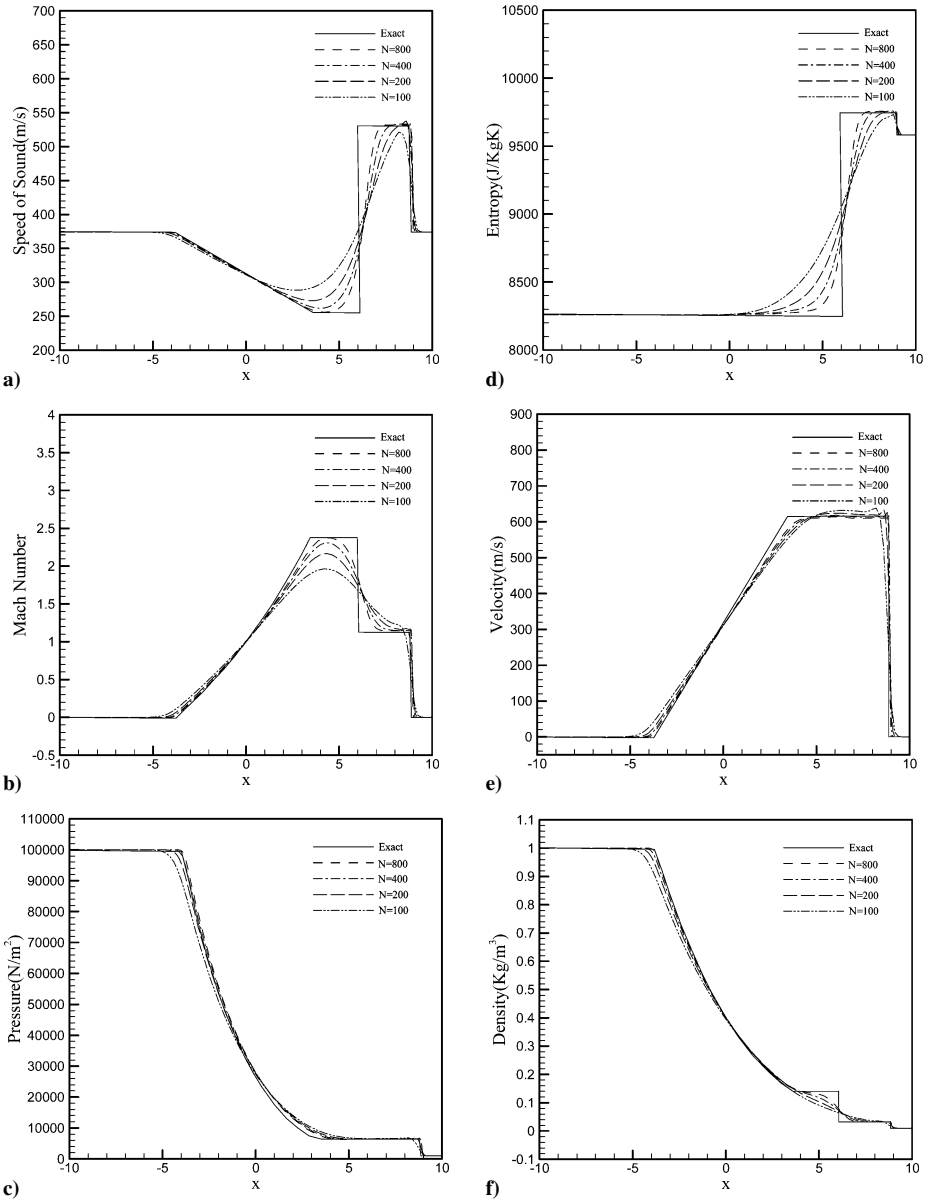

Fig. 7 Structure of flowfield at $t = 0.01$ for test case 2.

shown in Fig. 8d. The separation point of the flow for the present computation is at $x = 0.89$, which matches exactly with that predicted in Ref. 7. Figures 9a and 9b show the variation of pressure and skin-friction coefficient on the solid surface, respectively. The results compare quite well with those obtained in Ref. 7.

This test problem proves the ability of the present scheme for the computation of flows that involve shock-wave/boundary-layer interaction, which is an important feature of compressible viscous flows.

The validation studies show that the PVU scheme is a stable and accurate scheme for computation of compressible flows governed by Euler and Navier–Stokes equations. Shocks and expansion waves are resolved quite well, and in the spatial domain close to shocks and expansion waves, no overshoots and undershoots are found when the PVU scheme is used. Typical flux schemes employ explicit artificial viscosity for stabilizing the flow. No such explicit addition is needed when the computation is carried out with the present scheme. Another major advantage of the PVU scheme is that for multidimensional flows it is simple and easy to implement. The state-of-the-art methods in Refs. 20 and 21 model both flux and wave interaction between families of waves. They employ flux vector splitting or Riemann solvers. However, for multidimensional flows these schemes are very costly, and their treatment of the flow near the boundaries is also very complex.

The main drawback of the PVU scheme is the use of first-order upwinding, which reduces the order of accuracy, particularly in regions of flow where the flow variables vary smoothly. Thus, a sufficiently fine grid is needed to overcome the effect of lower order of the local truncation error of the scheme. However, as suggested by Grotowsky and Ballmann,[8] incorporation of different constraints through flux limiters into numerical schemes, which are only active in regions of high gradient of flow variables, are no means for essential improvement. To achieve the physical limits, probably the resolution of the grid has to be increased. Based on the preceding arguments, it can be said that in terms of simplicity of application, especially for multidimensional flows, the PVU scheme exhibits good potential.

VI. Results and Discussion

A. Forward-Facing Step

Figure 10 shows the computational domain and boundary conditions for the forward-facing step. The solution domain has been selected in such a fashion so that it includes all of the essential features that are developed due to the presence of a forward-facing step such as shock/boundary-layer interaction and shock–shock interaction. The uniform freestream is aligned with the positive x axis. Instead of starting the solution with known boundary layer on the flat plate, the boundary layer is allowed to develop with time. As

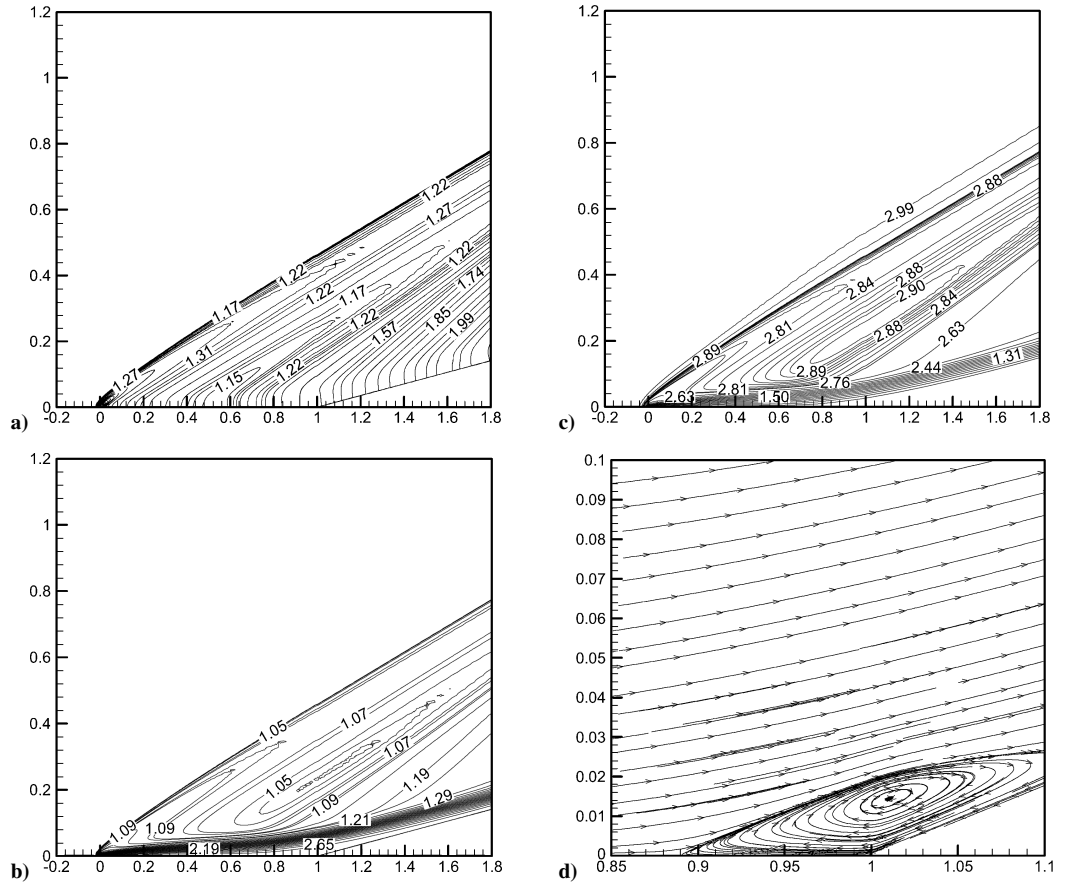

Fig. 8 Flow past 10-deg compression corner at $M_\infty = 3.0$: a) pressure contours, b) temperature contours, c) Mach contours, and d) streamtrace patterns.

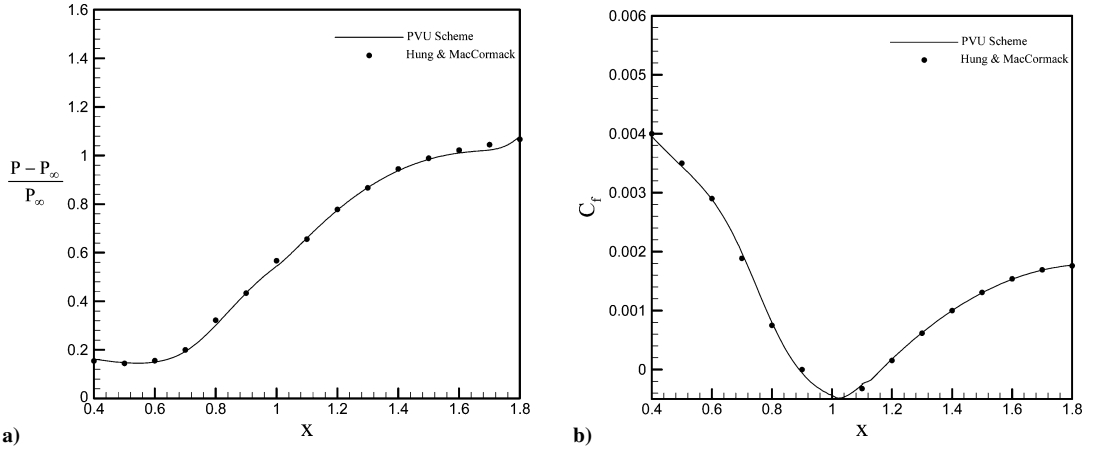

Fig. 9 Variation of a) pressure and b) skin-friction coefficient on the solid surface of the 10-deg compression corner at $M_\infty = 3.0$.

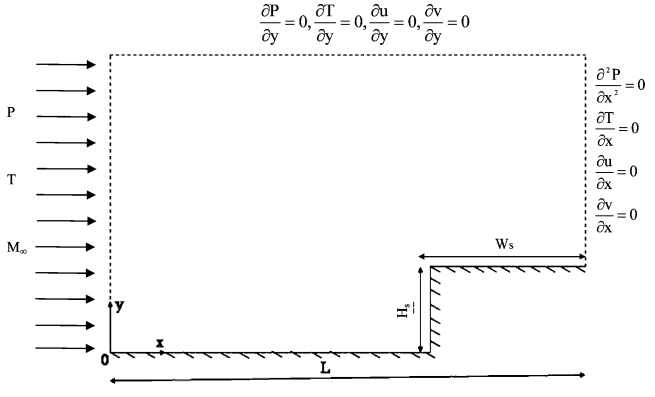

Fig. 10 Computational domain and boundary conditions.

a result, the leading-edge boundary-layer shock is generated. The leading edge is placed at $x = 0$, and the distance from the leading edge to the end of step L is used as the characteristic length.

At the inflow, pressure, temperature, and Mach number are specified at zero angle of attack. The no-slip condition for velocity is employed at the solid wall, and the wall static temperature is taken to be equal to the freestream air static temperature. The pressure at the solid wall is computed by using the normal momentum equation. At the outflow boundary, the second derivative of pressure and the first derivatives of temperature and velocity are set to zero, normal to the boundary. At the top boundary, the first derivatives of all of the flowfield variables, ρ, u, v, and T, in the y direction are assumed to be vanishing.

Based on the preceding validation, the PVU scheme in Sec. III is applied to the forward-facing step problem. A Newtonian fluid (air) with a calorically perfect gas assumption is used for the

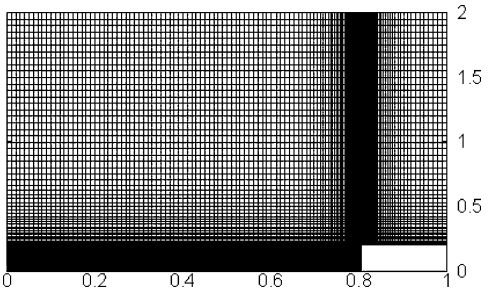

Fig. 11 Computational grid structure.

solution of the full conservative form of the Navier–Stokes equation. This problem comprises many parameters that can be varied. The freestream Mach number M_∞ and the nondimensional step height, $H = H_s/L$, appear to be important parameters that may affect the flowfield around the forward-facing step significantly. Thus, the numerical study involves the variation of Mach number M_∞ in supersonic ranges from 1.5 to 3.5 in steps of 0.5 for two step heights $H = 0.1$ and $H = 0.2$, respectively. The freestream Reynolds number Re_∞ based on the characteristic length is taken to be equal to 10^4, which corresponds to the laminar regime as shown by the transition studies of Chapman et al.[3] The numerical values of other parameters are as follows: $P_\infty = 101{,}325$ N/m^2, $T_\infty = 288$ K, $\gamma = 1.4$, $R = 287$ J/(kg · K), and $Pr_\infty = 0.716$.

Figure 11 shows the computational grid used for calculation. A fine (order 10^{-4}) nonuniform mesh spacing is used in the region near the wall for resolving the viscous layer, and a coarse (order 10^{-2}), equally spaced mesh is used in the outer region, where viscous effects are negligible. For the problem considered, a series of grid-refinement calculations are carried out to assess the grid size effect on the accuracy of results. The flow parameters are the same as already discussed. The grid points both in the x and y directions are changed, and the effect on wall pressure and skin friction is observed at $M_\infty = 3.0$ and $H = 0.1$ for three different grids, 111×116, 149×163, and 169×181. The percentage difference for first two grid is of 5%, whereas for last two grids it is only 2%. Hence, for the computations, the 149×163 grid is used. For this grid, the minimum spacing in the x and y directions is $\Delta x_{\min} = 0.001$ and $\Delta y_{\min} = 0.0008$, respectively. The nondimensional time step is taken to be 8×10^{-5}.

B. Spatial Patterns of the Flowfield

Figure 12 is a schematic diagram for the flow features that are developed due to the presence of forward-facing step. The spatial pattern of the flowfield is studied by plotting contours of pressure, temperature, Mach number, and streamtrace patterns at $H = 0.1$ and $M_\infty = 2.5$ in Figs. 13a–13d, respectively. A boundary layer starts developing from the leading edge of the plate, which decelerates the incoming supersonic flow for $x \geq 0$. A weak boundary-layer shock originates from the leading edge of the boundary layer as seen in Fig. 13a. Furthermore, all of the compression waves in front of the step merge, leading to a strong oblique shock in front of the step, which can be clearly seen in Fig. 13a. The strong oblique shock merges with the weak leading boundary-layer shock, causing a shock–shock interaction. The interaction is classified by Edney[22] as type IV interaction in which, after the intersection of two shocks, a single strong shock emerges followed by formation of a weak expansion wave and a slip surface. The slip surface formed due to the shock interaction is a contact discontinuity. In multidimensional flows, the contact discontinuities often occur in the form of slip lines or vortex sheet, as discussed in Ref. 9. The strong oblique shock interacts with the boundary layer in the viscous region near the wall and induces boundary-layer separation. The region between the strong oblique shock and the step face is the region of separation, dominated by the presence of a vortex as seen in Fig. 13d.

The temperature contours in Fig. 13b indicate the rise in temperature in the vicinity of the shocks. However, a higher temperature rise is observed near the solid boundary and the corner. This is because

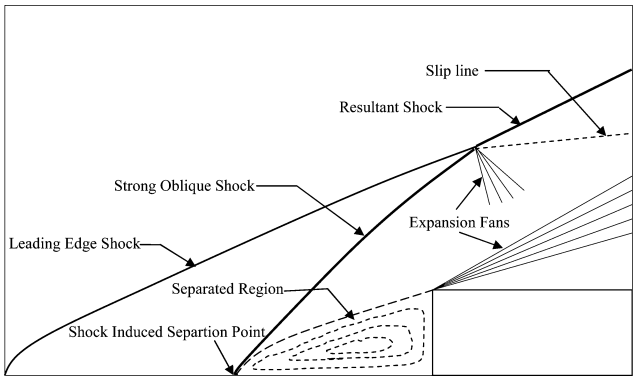

Fig. 12 Schematic diagram of spatial flow features for supersonic flow past forward-facing step.

the incoming freestream with high kinetic energy dissipates energy due to a strong viscous action near the wall.

The Mach contours in Fig. 13c are characterized by a thick band, starting from leading edge to the corner of the step. The thick band is the shear layer, which is the region between the outer nearly uniform high-speed flow and the slow-moving recirculating or separated region. This causes a high velocity gradient in the layer, which appears as thick band of concentrated Mach contours.

C. Effect of Step Height

The effect of step height on the spatial patterns of the flowfield can be assessed by comparing the spatial patterns in Figs. 13a–13d to those of Figs. 14a–14d, which correspond to spatial patterns of $H = 0.2$ and $M_\infty = 2.5$. Comparing the pressure contours plots in Figs. 13a and 14a, one can conclude that, as the step height increases, the strong oblique shock moves toward the leading edge and merges with the weak leading-edge boundary-layer shock, causing shock interactions. The pressure variations in front of the step and on step face (Figs. 15a and 15b) are compared for the two step heights at $M_\infty = 2.5$. The separated region has a plateau of nearly constant pressure (except near the step corner) representing a dead air region, as seen in Fig. 15a. The separation point pressure and the plateau pressure increase as the step height increases, with respect to the freestream pressure. The sudden pressure rise in front of the step is an indicator of the location of the oblique shock. Thus, it is clear from Fig. 15a that the oblique shock moves toward the leading edge as the height is increased.

Near the step, a small pressure rise is observed in the lower corner of the step because a portion of the separated layer is brought to rest on the step face. A study of pressure variation along the vertical face of the step (Fig. 15b) indicates the following features. There is a region extending from the lower corner to around the middle of the step where the pressure is almost constant. From the middle of the step to the top corner there is a monotonic rise. At the top of the face, there is an abrupt fall indicating presence of an expansion region on the shoulder of the step. It is seen from both Figs. 15a and 15b that the pressure magnitude in front of the step and on the step face are altered significantly with increase in step height. Figure 15c shows the wall variations of coefficient of skin friction for the two step heights. The point nearest to the leading edge, where the coefficient of skin friction becomes negative, indicates the beginning of the separation region. Thus, as the step height increases, the separation point shifts toward the leading edge, and, hence, the length of separated region increases with step height. The skin friction near the step changes from negative to positive and back again to negative. This is due to the presence of small secondary vortex at the corner of the step (Fig. 13d), which circulates in the opposite sense to that of the primary vortex, causing positive shear. For $H = 0.2$, the skin friction is positive in two regions in the separated zone because of the presence of two secondary vortices in the flowfield as seen in Fig. 14d.

Figure 15d shows the Stanton number for the isothermal wall as a function of distance from the leading edge to the step base for

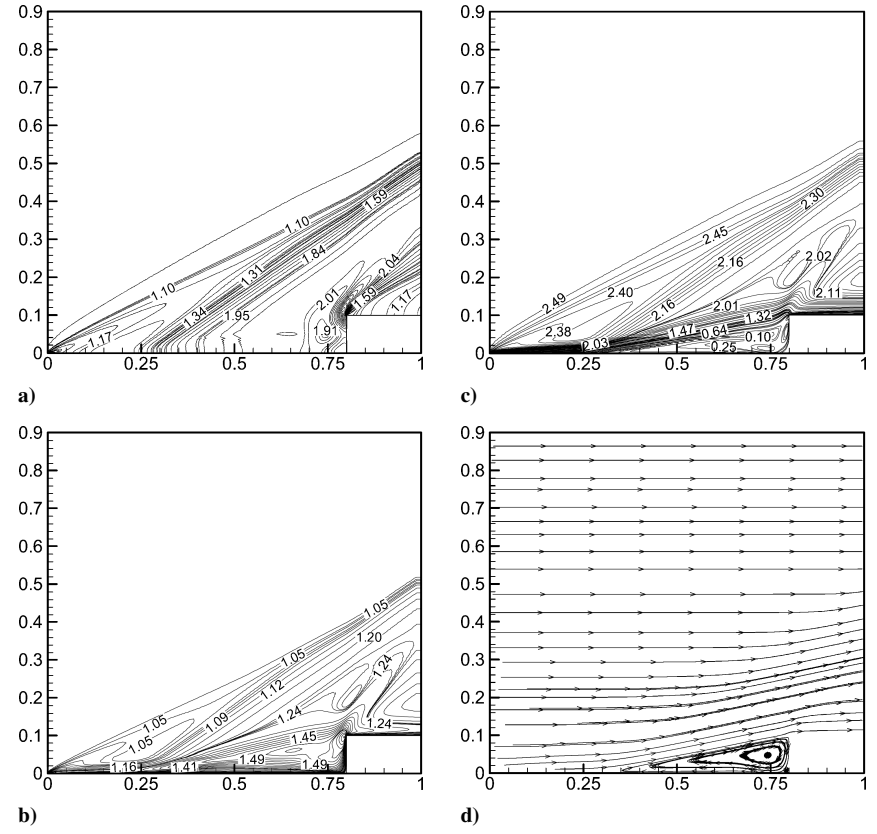

Fig. 13 Flow past the forward-facing step at $M_\infty = 2.5$ and $H = 0.1$: a) pressure contours, b) temperature contours, c) Mach contours, and d) streamtrace patterns.

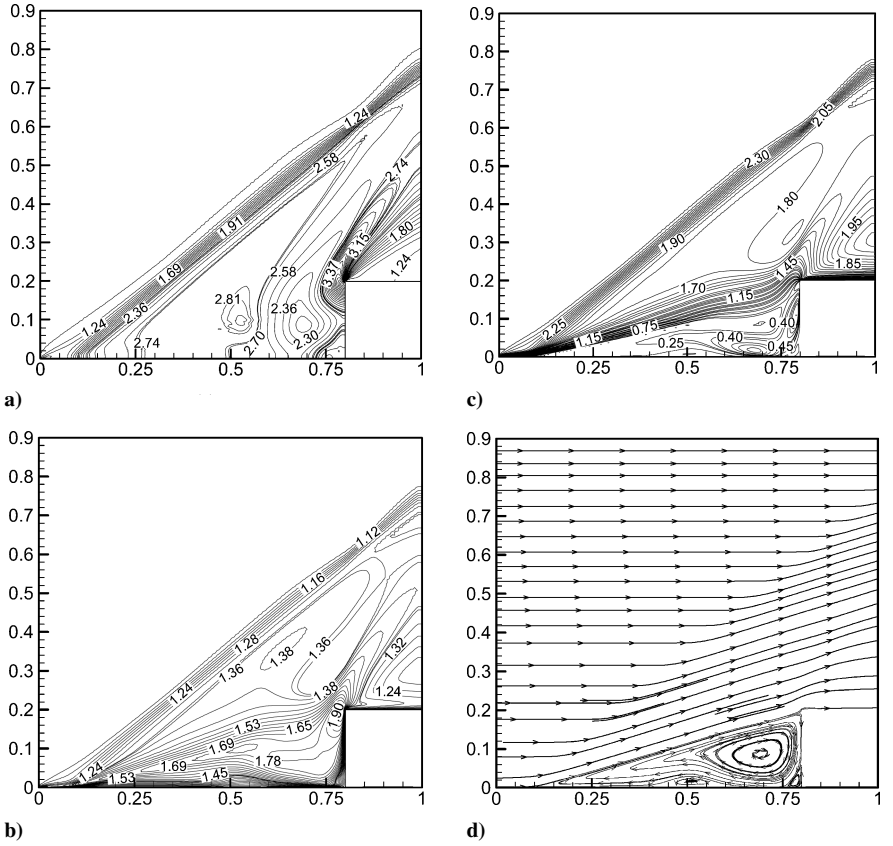

Fig. 14 Flow past the forward-facing step at $M_\infty = 2.5$ and $H = 0.2$: a) pressure contours, b) temperature contours, c) Mach contours, and d) streamtrace patterns.

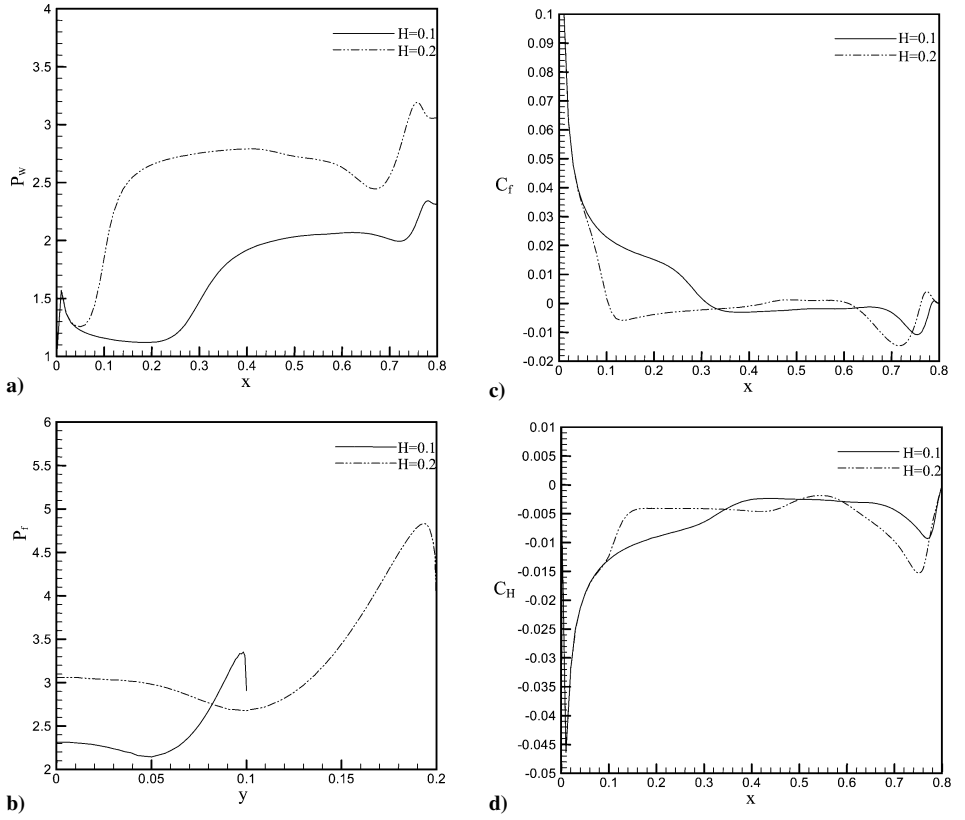

Fig. 15 Profiles of a) pressure on horizontal wall, b) pressure on vertical step face, c) skin-friction coefficient on horizontal wall, and d) Stanton number for $y = 0$ and $M_\infty = 2.5$ at different step heights.

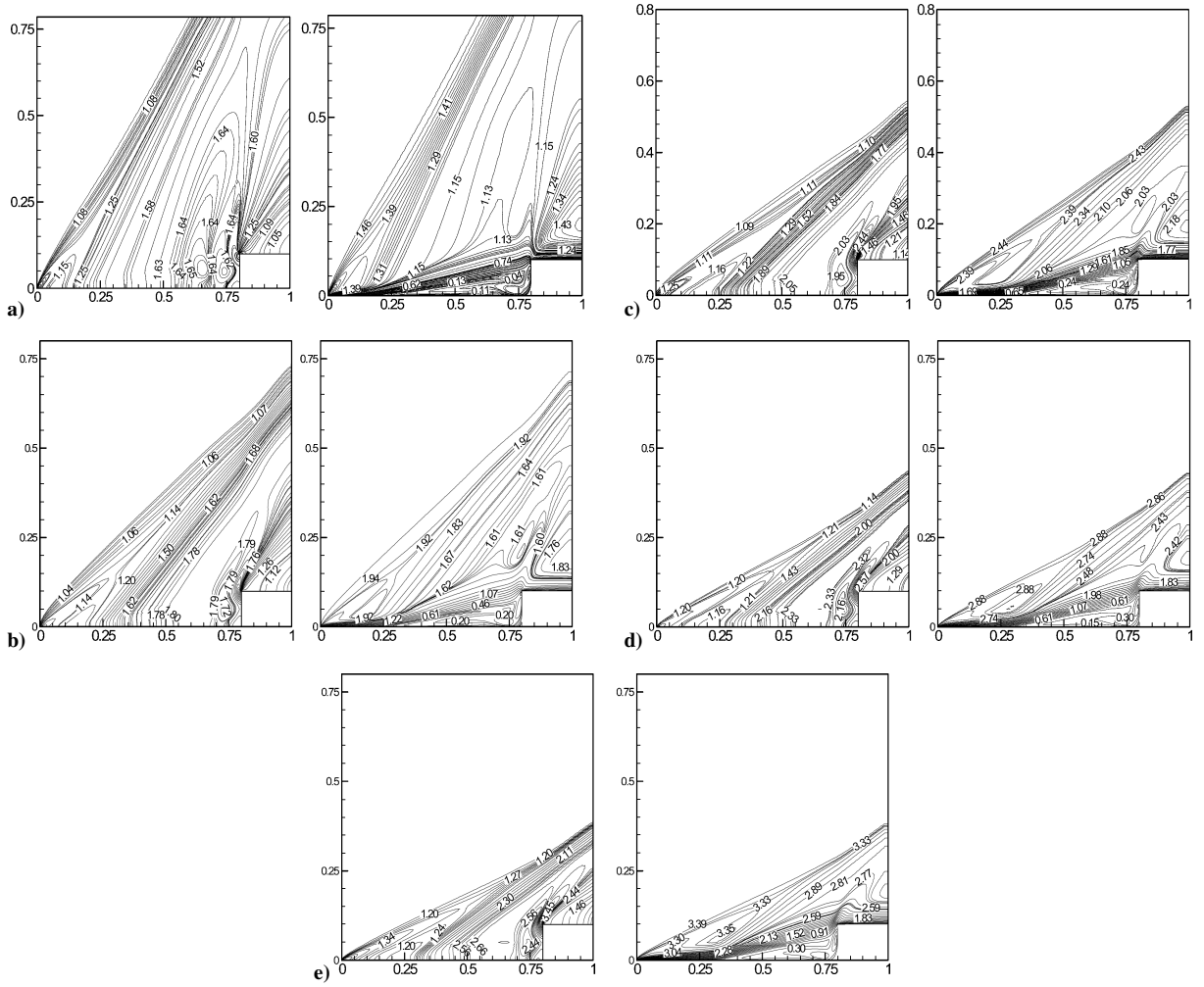

Fig. 16 Pressure and Mach contours at a) $M_\infty = 1.5$, b) $M_\infty = 2.0$, c) $M_\infty = 2.5$, d) $M_\infty = 3.0$, and e) $M_\infty = 3.5$ for $H = 0.1$.

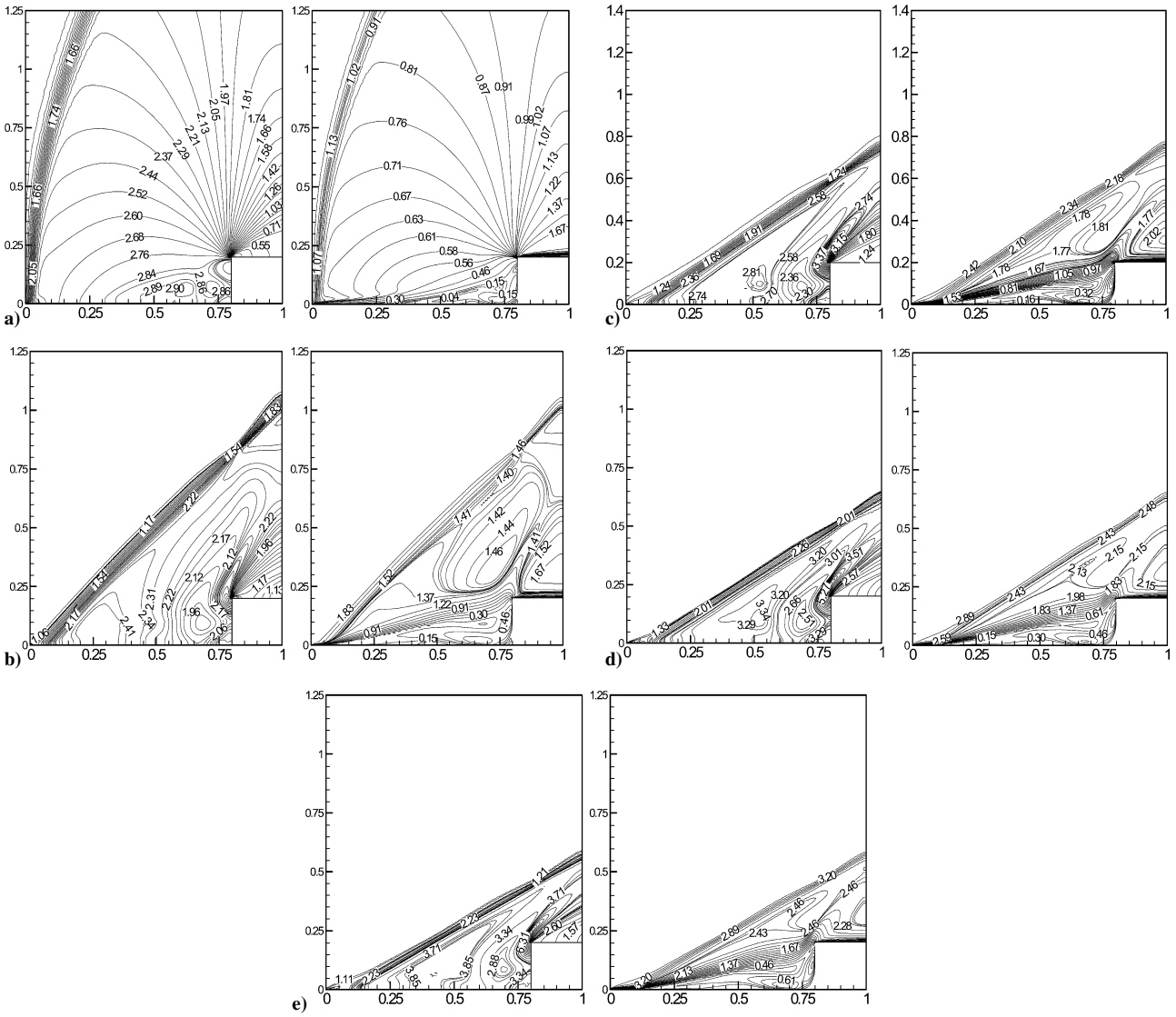

Fig. 17 Pressure and Mach contours at a) $M_\infty = 1.5$, b) $M_\infty = 2.0$, c) $M_\infty = 2.5$, d) $M_\infty = 3.0$, and e) $M_\infty = 3.5$ for $H = 0.2$.

the two step heights at $M_\infty = 2.5$. The negative values indicate that heat is being transferred from the fluid to the solid surface. The heat transfer rate decreases from the leading edge to the separation point. In the separation zone, it almost stays constant and increases near the step. The same trend is observed for both the step heights.

D. Effect of Freestream Mach Number

Figures 16a–16e show the pressure and Mach contours for different Mach numbers at $H = 0.1$. The increase in Mach number reduces the inclination of both the leading edge and the strong oblique shocks. It is also observed that the increase in Mach number pushes the oblique shock away from the leading edge toward the step. At $H = 0.2$, Figs. 17a–17e show similar trends in the change in the spatial pattern of flow as Mach number is increased. However, at $H = 0.2$, the distance between the leading edge shock and the oblique shock is much less. In fact, at low Mach number $M_\infty = 1.5$ (Fig. 17a), the leading-edge shock and the oblique shock coalesce to form a single nearly normal shock at the leading edge. As M_∞ is increased, the two shocks separate and the oblique shock starts to move away from the leading edge toward the step.

Figures 18a–18c show the variation of static pressure, skin friction, and Stanton number, respectively, at $H = 0.1$ as a function of distance from leading edge to the step base at the wall. The movement of the oblique shock and the associated separation point, away from the leading edge, toward the step is clearly seen. The effect of Mach number is more pronounced in wall static pressure than in skin friction C_f and Stanton number C_H. The separated zone pressure is significantly increased with increase in freestream Mach number. This is because the strength of the oblique shock increases as the freestream Mach number is increased.

Figures 19a–19c show the wall variation of static pressure, skin friction, and Stanton number at $H = 0.2$. At this height, the trend is similar to that at $H = 0.1$ for M_∞ variation between 2 and 3.5. However, at $M_\infty = 1.5$, the wall pressure and length of the separation zone are greater than those for $M_\infty = 2$ and $M_\infty = 2.5$. This is due to the coalescence of the leading edge and the oblique shock at $M_\infty = 1.5$ to form a strong nearly normal shock at the leading edge. The wall variation of static pressure at $H = 0.2$ also indicates that the level of the pressure rise after the oblique shock is much higher than for the case of $H = 0.1$.

Figures 20a and 20b show the variation of peak pressure on step face and length of the separated region, measured from the step, with Mach number at the two step heights. The peak pressure on the step face increases with an increase in M_∞ for both step heights. The increase is quite large as the peak pressure is nearly quadrupled for both the step heights, with increase in M_∞ from 1.5 to 3.5. In contrast, the separated region length decreases only slightly (by about 16% at $H = 0.1$ and about 7% at $H = 0.2$) with an increase in M_∞ from 1.5 to 3.5. Because separation is induced by the oblique shock, it can also be inferred that there is a very slight shift in the location of the shock toward the step as M_∞ is increased from 1.5 to 3.5. However, the separated region length is altered quite significantly with step height, with an increase of approximately 25–50% for the entire range of M_∞.

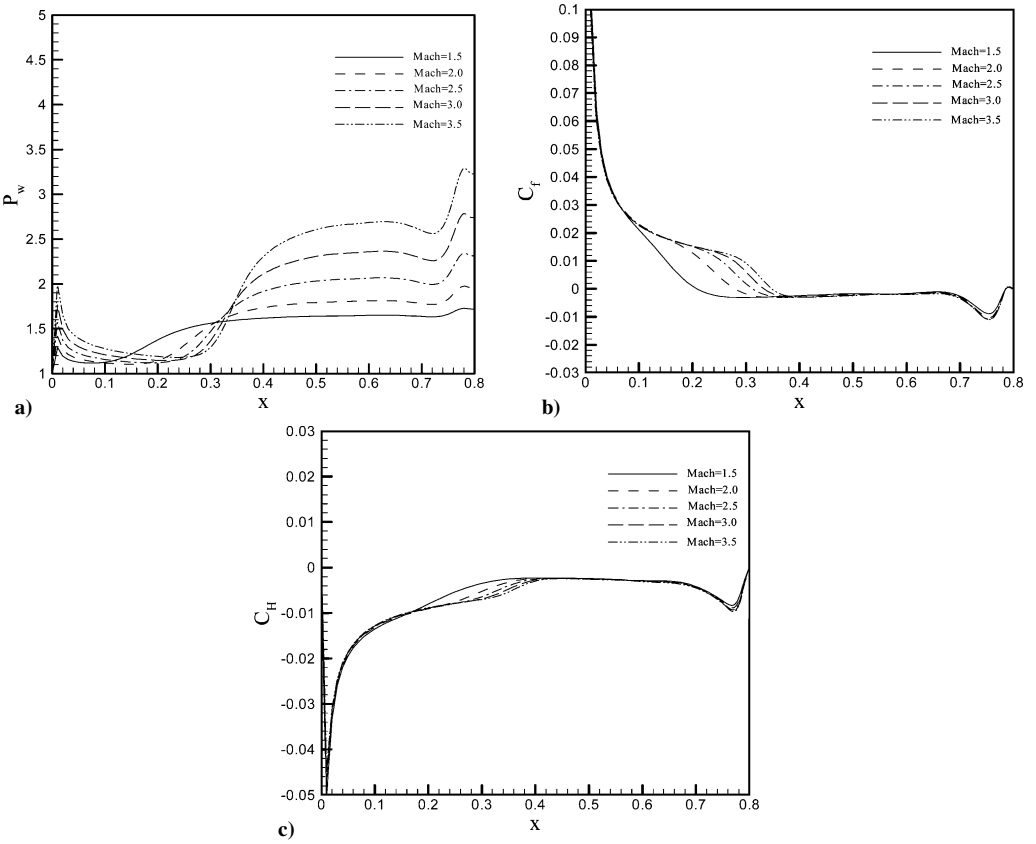

Fig. 18 Profiles of a) pressure on horizontal wall, b) skin-friction coefficient on horizontal wall, and c) Stanton number at $y = 0$ and $H = 0.1$ for different Mach numbers.

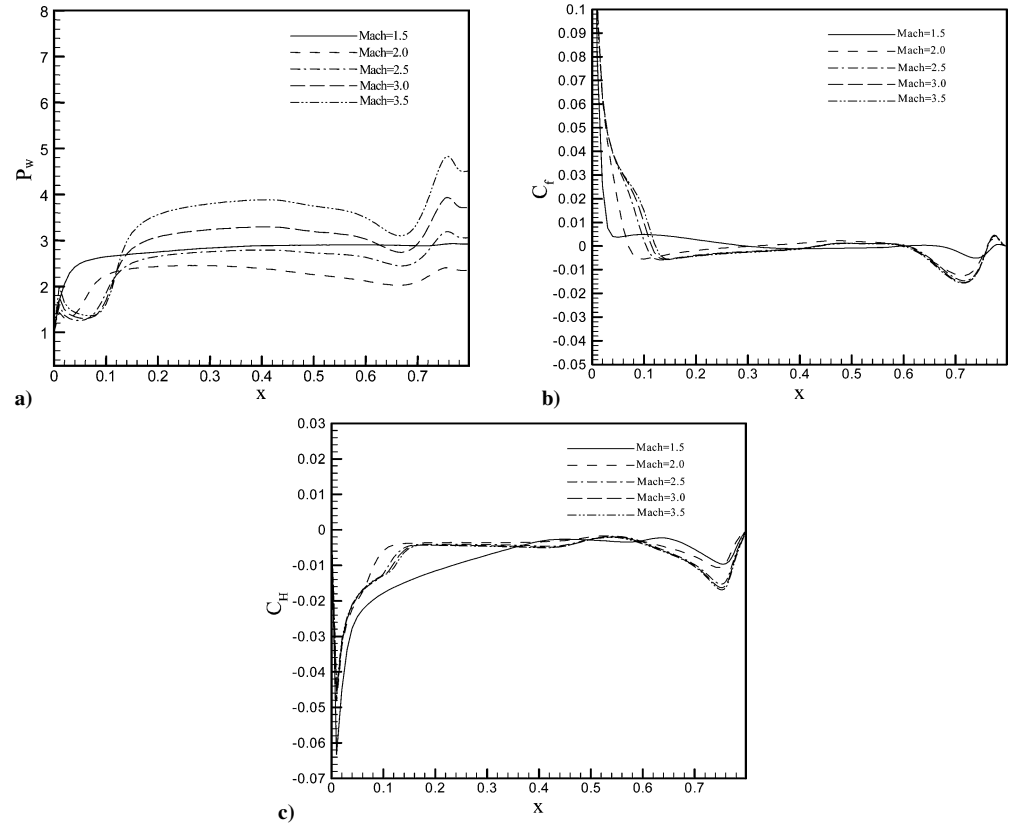

Fig. 19 Profiles of a) pressure on horizontal wall, b) skin-friction coefficient on horizontal wall, and c) Stanton number at $y = 0$ and $H = 0.2$ for different Mach numbers.

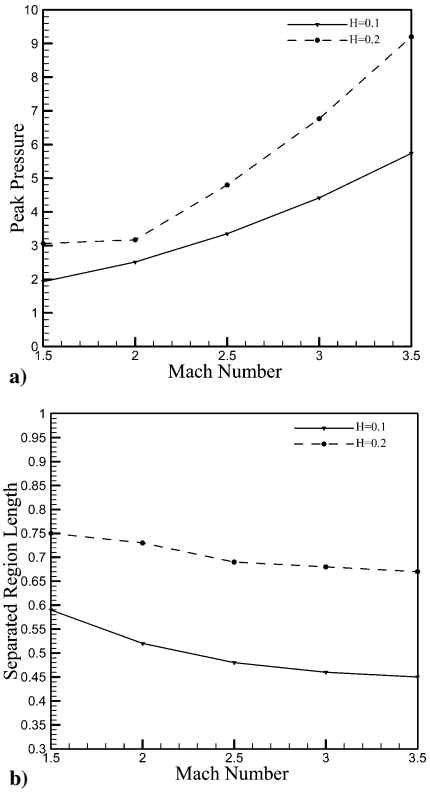

Fig. 20 Variation of a) Peak pressure on vertical step face and b) separated region length with Mach number for $H = 0.1$ and $H = 0.2$.

VII. Conclusions

In this work, a numerical scheme is introduced that is a modified version of the commonly used flux-based predictor–corrector schemes. The proposed PVU scheme is a simple, reasonably accurate, and stable scheme for the computation of multidimensional, high-speed, compressible flows. This scheme is used to study the supersonic flow past a forward-facing step. The salient features of the flow are the leading-edge weak shock, a strong oblique shock in front of the step, the separation induced by the oblique shock, and the intersection of leading-edge shock with the oblique shock giving rise to a shock–shock interaction. From the parametric study carried out for the forward-facing step problem, it can be concluded that the strength and the location of the oblique shock are affected by two parameters: 1) the freestream Mach number M_∞ and 2) the step height H. It is also shown that the shock strength is significantly affected by the step height, as well as the freestream Mach number. However, the shock location is altered significantly only by the step height. It does not change much as the Mach number is varied. Consequently, the wall static pressure in front of the step and on the step face is affected significantly by both the parameters M_∞ and H. However, the skin friction C_f and wall heat transfer C_H are affected significantly by step height only and not by M_∞. Thus, from the design point of view, although the separated zone and the step face pressures can be effectively controlled by the freestream Mach number and the step height, the shock location/length of separated zone is controlled more effectively by the step height.

The PVU scheme is first-order accurate in space and second-order accurate in time. The spatial accuracy of the scheme can be improved by employing high-order finite difference approximations throughout the solution domain. However, an increase in the spatial order of accuracy may lead to the phenomena of Gibbs oscillations, especially near discontinuities. Thus, to increase the spatial order of accuracy in the smooth region of the flowfield and to avoid oscillations near discontinuities, one needs to employ a solution sensitive strategy. In this strategy, first-order accurate discretization in the regions of steep gradients (regions containing the discontinuities) and higher-order discretization in the smooth region of the flow may be employed. To achieve this, first a strategy for detecting regions of steep gradients must be devised. Once the region of steep gradient is identified in the flowfield, a first-order upwinding procedure on the convective terms can be applied in that region, and in the remaining region (smooth region), a higher-order upwinding procedure is applied to the convective term. This can improve the overall spatial accuracy of the scheme. In this paper, only the first-order accurate form of the PVU scheme is demonstrated; the higher-order accurate form of the PVU scheme will be discussed in future works.

References

[1]Lees, L., and Reeves, B. L., "Supersonic Separated and Reattaching Laminar Flow: I. General Theory and Application to Adiabatic Boundary Layer Shock/Wave Interaction," *AIAA Journal*, Vol. 2, No. 11, 1964, pp. 1907–1920.

[2]Klinberg, J., and Lees, L., "Theory of Laminar Viscous-Inviscid Interaction in Supersonic Flows," *AIAA Journal*, Vol. 7, No. 12, 1969, pp. 2211–2221.

[3]Chapman, D. R., Kuehn, D. M., and Larson, H. K., "Investigation of Separated Flows in Supersonic and Subsonic Streams with Emphasis on the Effect of Transition," NACA TR1356, 1957.

[4]Li, S., Chen, Y., and Ni, Z., "Pressure Measurement and Flow Visualization on Hypersonic Flow over Rectangular Cylinder," *6th FLUCOME International Symposium on Fluid Control, Measurement and Visualization*, Paper CD-129, Transvision Rèseau, Inc., Sherbroke, Canada, 2000.

[5]Efimtsov, B. M., Rizzi, S. A., Andersson, A. O., and Andrianov, E. V., "Influence of Small Steps on Wall Pressure Fluctuation Spectra Measured on TU-144LL Flying Laboratory," AIAA Paper 2002-2605, June 2002.

[6]Carter, J. E., "Numerical Solution of the Navier–Strokes Equation for the Supersonic Laminar Flow over Two Dimensional Compression Corner," NASA TR R-385, 1972.

[7]Hung, C. M., and MacCormack, R. W., "Numerical Solutions of Supersonic and Hypersonic Laminar Compression Corner Flows," *AIAA Journal*, Vol. 14, No. 4, 1976, pp. 475–481.

[8]Grotowsky, I. M. G., and Ballmann, J., "Numerical Investigation of Hypersonic Step-Flow," *Shock Waves*, Vol. 10, No. 29, 2000, pp. 57–72.

[9]Laney, C. B., *Computational Gasdynamics*, Cambridge Univ. Press, Cambridge, England, U.K., 1998.

[10]Anderson, J. D., *Computational Fluid Dynamic*, McGraw–Hill, New York, 1995.

[11]Toro, E. F., *Riemann Solvers and Numerical Methods for Fluid Dynamics*, 2nd ed., Springer, Berlin, 1999.

[12]Sod, G. A., "A Survey of Several Finite Difference Methods for Systems of Nonlinear Hyperbolic Conservation Laws," *Journal of Computational Physics*, Vol. 27, No. 1, 1978, pp. 1–31.

[13]Harten, A., "High-Resolution Schemes for Hyperbolic Conservation Laws," *Journal of Computational Physics*, Vol. 49, No. 3, 1983, pp. 357–393.

[14]Van Leer, B., Lee, W. T., and Powell, K. G., "Sonic Point Capturing," *Proceedings of the AIAA 9th Computational Fluid Dynamics Conference*, AIAA, Washington, DC, 1989, pp. 176–187.

[15]Van Leer, B., "Flux Vector Splitting for the Euler Equations," *8th International Conference of Numerical Methods in Fluid Dynamics, Lecture Notes in Physics*, Vol. 170, Springer-Verlag, Berlin, 1989, pp. 507–512.

[16]Roe, P. L., "Approximate Riemann Solver, Parameter Vectors, and Difference Schemes," *Journal of Computational Physics*, Vol. 43, No. 2, 1981, pp. 357–372.

[17]Gudunov, S. K., "A Different Scheme for Numerical Computation of Discontinues Solution of Hydrodynamics Equations," U.S. Joint Publications Research Service, Rept. JPRS7226, New York, 1969.

[18]Mittal, S., and Yadav, S., "Computation of Flows in Supersonic Wind-Tunnels," *Computer Method in Applied Mechanics and Engineering*, Vol. 191, No. 6–7, 2003, pp. 611–634.

[19]Shakib, F., "Finite Element Analysis of the Compressible Euler and Navier–Stokes Equation," Ph.D. Dissertation, Dept. of Mechanical Engineering, Stanford Univ., Stanford, CA, 1988.

[20]Harten, A., Engquist, B., Osher, S., and Chakarvarthy, R. S., "Uniformly High Order Accurate Essentially Non-Oscillatory Scheme," *Journal of Computational Physics*, Vol. 71, No. 2, 1987, pp. 231–303.

[21]Liu, X. D., Osher, S., and Chan, T., "Weighted Essentially Non-Oscillatory Scheme," *Journal of Computational Physics*, Vol. 115, No. 1, 1994, pp. 200–212.

[22]Edney, B., "Anomalous Heat Transfer and Pressure Distributions on Blunt Bodies at Hypersonic Speeds in Presence of an Impinging Shock," Aeronautical Research Inst. of Sweden, Rept. FFA116, Stockholm, Feb. 1968.

C. Kaplan
Associate Editor